Chaotic mixing induced by a magnetic chain in a rotating magnetic field

Tae Gon Kang, Martien A. Hulsen,* Patrick D. Anderson, Jaap M. J. den Toonder, and Han E. H. Meijer
Materials Technology, Eindhoven University of Technology, P.O. Box 513, 5600 MB Eindhoven, The Netherlands
(Received 21 August 2007; published 6 December 2007)

Chaotic mixing, induced by breakup and reformation of a magnetic chain under the influence of a rotating magnetic field, is studied. A direct simulation method combining the Maxwell stress tensor and a fictitious domain method is employed to solve flows with suspended magnetic particles. The motion of the chain is significantly dependent on the Mason number (Ma), the ratio of viscous force to magnetic force. The degree of chaos is characterized by the maximum Lyapunov exponents. We also track the interface of two fluids in time and calculate the rate of stretching as it is affected by the Mason number. The progress of mixing is visualized via a tracer particle-tracking method and is characterized by the discrete intensity of segregation. Within a limited range of Mason number, a magnetic chain rotates and breaks into smaller chains, and the detached chains connect again to form a single chain. The repeating topological changes of the chain lead to the most efficient way of chaotic mixing by stretching at chain breakup and folding due to rotational flows.

DOI: 10.1103/PhysRevE.76.066303 PACS number(s): 47.51.+a, 47.61.−k, 83.80.Gv, 47.11.−j

I. INTRODUCTION

The area of micro-total-analysis systems (μ-TAS) [1], also known as lab-on-a-chip, integrating laboratory functions in biology and chemistry on a single chip and handling extremely small fluid volumes, has been recently growing rapidly. The increasing interest in μ-TAS has stimulated the development of microfluidic components like valves, pumps, mixers, reactors, sensors, and actuators to achieve better and more dedicated performance, satisfying specific requirements in different application areas [2]. One of the key components in the system is a micromixer [3] to which the theory of chaotic mixing [4,5] has been recently extensively applied to achieve enhanced mixing. Under typical operating conditions, flows in these devices are laminar and molecular diffusion across the microchannels is slow, which makes an efficient mixing in microfluidic devices difficult to achieve.

Since the appearance of the concept of μ-TAS, suspensions of magnetic particles are being used in microfluidics for chemical or biomedical applications [6,7]. Mostly, magnetic particles are used as mobile substrates for bio-assays to be transported to the desired locations [8,9] or as stirring agents to achieve enhanced mixing [9,10]. When exposed to uniform magnetic fields externally applied, magnetically polarizable particles acquire dipole moments and the induced moments interacting with each other lead to the formation of chainlike structures or clusters of particles aligned with the field direction. As for the effect of rotating magnetic fields on the dynamics of magnetic chains, several experimental studies showed that the structure and dynamics of chains are influenced by the frequency of the fields [11–14]. Recently, Calhoun *et al.* [15] studied mixing by a magnetic chain in a rotating magnetic field using a numerical scheme based on the lattice Boltzmann method (LBM) and the dipole-dipole interaction model. They claimed that mixing is highly affected by a dimensionless number called the Mason number, the ratio of viscous force to magnetic force, and showed the existence of an optimal Mason number for enhanced mixing using the standard deviation of a scalar concentration of a circular blob. However, their mixing analysis is based on a local measure of mixing, which is not relevant to an in-depth mixing analysis and requires further investigation. Motivated by these works, in this study, we investigate the use of magnetic chains formed by paramagnetic particles as active microstirrers for microfluidic mixing, which have attractive applications in diagnostic lab-on-a-chip devices.

As a fundamental study of chaotic mixing, induced by a magnetic chain under the influence of a rotating magnetic field, we aim to investigate the dynamics of the chain, the flow characteristics induced, and the subsequent mixing in detail. For these purposes, we employ a direct numerical simulation method [16], which is based on a fictitious domain method [17] and the finite-element method. The forces resulting from magnetic interactions between particles are implemented through the Maxwell stress tensor [18,19], which is a different approach from the dipole-dipole interaction model [12,15]. The numerical method enables us to take into account both hydrodynamic and magnetic interactions in a fully coupled manner. As a model problem, we choose a two-dimensional (2D) liquid-filled circular cavity with suspended circular paramagnetic particles, initially forming a chain, under the influence of a rotating magnetic field.

The paper is organized as follows. First, we introduce the problem and the governing equations to solve the problem, resulting in the final weak formulations of the finite-element method. Then, the dynamics of the chain and the characteristics of the induced flow, influenced by topological changes such as breakup and reformation of the chain, will be discussed with an emphasis on the effect of the Mason number. The degree of chaos in the cavity is characterized by the maximum Lyapunov exponents. We also track the interface of two fluids to show detailed deformation patterns with flow. Finally, we show the progress of mixing via interface tracking and colored tracer particle tracking. Chaotic mixing dependent on the Mason number is characterized using a measure of mixing, called the discrete intensity of segregation, based on the distribution of the tracer particles throughout the whole fluid domain.

*Corresponding author: m.a.hulsen@tue.nl

 ©2007 The American Physical Society

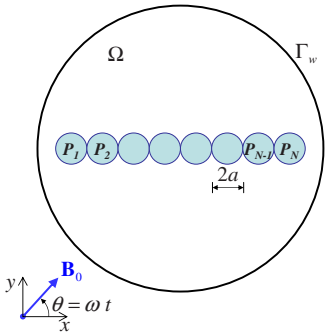

FIG. 1. (Color online) Schematic representation of a magnetic chain, formed by N circular particles with the radius a, suspended in a two-dimensional liquid-filled circular cavity under the influence of a rotating magnetic field. The magnetic field is rotating with a constant angular frequency ω. The whole cavity is denoted by Ω and the boundary of the cavity is denoted by Γ_w.

II. MODELING

A. Problem definition

As depicted in Fig. 1, the problem chosen is flow in a two-dimensional liquid-filled circular cavity with N paramagnetic particles, subjected to a rotating magnetic field, initially forming a chain aligned horizontally with its center at the cavity center. The particles are circular with the same radius a. In this circular cavity, the hydrodynamic interaction between the cavity wall and the chain is independent of the angular position of the chain. We use a symbol $P(t)$ for $\cup_{i=1}^{N} P_i(t)$ as a collective region occupied by particles at a certain time t. The fluid domain is denoted by $\Omega \backslash P(t)$ with the whole domain being Ω. The externally applied magnetic field is the only driving force to actuate particles and subsequently to induce flow. In this case, the magnetic flux density $\boldsymbol{B}_0$ on the cavity boundary has the form $\boldsymbol{B}_0 = B_0[\cos(\omega t)\boldsymbol{e}_x + \sin(\omega t)\boldsymbol{e}_y]$, where B_0 is the magnitude of the magnetic flux density, ω the angular frequency of the rotating field, and t the time. Thus, the strength of the magnetic field applied externally is constant, but the direction of the field is changing with a constant angular frequency ω.

The fluid is assumed to be nonmagnetic with a magnetic permeability μ_0 and a constant viscosity η. The fluid flow is assumed to be governed by viscous forces and magnetic interactions between particles, neglecting effects of inertia. The particles are assumed to be non-Brownian, inertialess, and paramagnetic with a constant permeability μ_p, but they do interact with each other via hydrodynamic and magnetic interactions. The particles are magnetically neutral in the absence of a magnetic field applied externally, but magnetized under the influence of an external magnetic field. A linear relation between $\boldsymbol{B}$ and $\boldsymbol{H}$ is assumed, neglecting magnetic saturation, which is an approximation for relatively small field strengths.

B. Magnetic problem

We assume that the magnetic field is governed by magnetostatics, for which the governing Maxwell equations are written as

$$\nabla \times \boldsymbol{H} = \boldsymbol{J}, \tag{1}$$

$$\nabla \cdot \boldsymbol{B} = 0, \tag{2}$$

where $\boldsymbol{H}$ is the magnetic field intensity, $\boldsymbol{J}$ the current density, and $\boldsymbol{B}$ the magnetic flux density. The constitutive equation relating $\boldsymbol{B}$ and $\boldsymbol{H}$ is $\boldsymbol{B} = \mu \boldsymbol{H}$, where μ denotes the magnetic permeability of a linear isotropic medium. In general, to solve the two Maxwell equations, the two first-order partial differential equations are converted into a second-order partial differential equation, involving only one field variable called the magnetic vector potential $\boldsymbol{A}$ [18]. The magnetic flux density is represented by the curl of the magnetic vector potential, i.e., $\boldsymbol{B} = \nabla \times \boldsymbol{A}$, which satisfies Eq. (2). Then, the resulting partial differential equation for $\boldsymbol{A}$ is given by

$$\nabla \times \left(\frac{1}{\mu} \nabla \times \boldsymbol{A} \right) = \boldsymbol{J}. \tag{3}$$

At a current-free interface between two media—for example, a fluid-particle interface with different magnetic permeabilities—the magnetic fields should satisfy two continuity equations, given by

$$\boldsymbol{n} \cdot (\boldsymbol{B}_\mathrm{f} - \boldsymbol{B}_\mathrm{p}) = \boldsymbol{0}, \tag{4}$$

$$\boldsymbol{n} \times (\boldsymbol{H}_\mathrm{f} - \boldsymbol{H}_\mathrm{p}) = \boldsymbol{0}, \tag{5}$$

where $\boldsymbol{n}$ is a unit vector normal to the interface pointing from the particle domain to the fluid and the variables with the subscript "f" and "p" represent those variables evaluated from the fluid domain and the particle domain, respectively. Equations (4) and (5) represent the continuity of the normal component of $\boldsymbol{B}$ and the tangential component of $\boldsymbol{H}$ at the interface.

In a two-dimensional Cartesian coordinate system, assuming a vertical current, $\boldsymbol{J} = J\boldsymbol{e}_z$, which is independent of the coordinate z, the governing equation in terms of the magnetic potential becomes

$$-\frac{\partial}{\partial x}\left(\frac{1}{\mu_r} \frac{\partial A}{\partial x} \right) - \frac{\partial}{\partial y}\left(\frac{1}{\mu_r} \frac{\partial A}{\partial y} \right) = \mu_0 J, \tag{6}$$

where μ_r denotes the relative permeability, $\mu_r = \mu / \mu_0$, and A the z component of the magnetic vector potential $\boldsymbol{A}$. Once the magnetic potential A is found, the components of the magnetic flux density, $\boldsymbol{B} = (B_x, B_y)$, are computed by

$$B_x = \frac{\partial A}{\partial y}, \quad B_y = -\frac{\partial A}{\partial x}. \tag{7}$$

The magnetic flux density is given at a cavity boundary as an essential boundary condition. Therefore, the values of the magnetic potential A may be explicitly defined at the boundary via a Dirichlet boundary condition. In a two-dimensional Cartesian coordinate system, the form of A at the boundary is specified by the parameters A_0, A_1, and A_2, as follows:

$$A = A_0 + A_1 x + A_2 y, \tag{8}$$

where A_0 is an arbitrary constant (here taken as zero, $A_0 = 0$). From Eq. (7), the two coefficients A_1 and A_2 are given by $A_1 = -B_{0y}$ and $A_2 = B_{0x}$ for the prescribed external flux density

$\boldsymbol{B}_0=(B_{0x},B_{0y})$. In terms of the magnetic potential A, the two continuity conditions at fluid-particle interfaces, Eqs. (4) and (5), are represented by

$$A_{\mathrm{f}}=A_{\mathrm{p}}, \tag{9}$$

$$\frac{1}{\mu_{rf}}\frac{\partial A_{\mathrm{f}}}{\partial n}=\frac{1}{\mu_{r\mathrm{p}}}\frac{\partial A_{\mathrm{p}}}{\partial n}, \tag{10}$$

where $\frac{\partial}{\partial n}=\boldsymbol{n}\cdot\boldsymbol{\nabla}$.

The body force $\boldsymbol{f}_{\mathrm{m}}$ experienced by materials in a magnetic field is represented by the divergence of the Maxwell stress tensor $\boldsymbol{T}_{\mathrm{m}}$, i.e., $\boldsymbol{f}_{\mathrm{m}}=\boldsymbol{\nabla}\cdot\boldsymbol{T}_{\mathrm{m}}$, where $\boldsymbol{T}_{\mathrm{m}}=\mu(\boldsymbol{HH}-\frac{1}{2}H^2\boldsymbol{I})$. Here, $\boldsymbol{f}_{\mathrm{m}}$ is regarded as a force density per volume (per area in the 2D case) exerted on the material body subjected to the magnetic field, which contributes to the momentum balance equation as an additional body force.

C. Flow problem

We assume that the fluid flow is governed by the Stokes equations. The particles are assumed to be force free and torque free, and the inertia of the particles is negligible. The force $\boldsymbol{f}_m$ working on magnetic particles is treated as a body force added to the momentum balance equation, as given in Eq. (11). As for the particle domain $P(t)$, we employ the rigid-ring description [17], where the same fluid as in the fluid domain also fills the particle domain and the rigid-body constraint is imposed on the particle boundaries only. This description enables us to solve the same governing equations for both (fluid and particle) domains, reducing the number of unknowns for the rigid-body constraints. It should be noted that the rigid-ring description is valid only for flows without inertia.

For the entire domain Ω, the set of equations describing the flow with rigid magnetic particles is represented by

$$-\boldsymbol{\nabla}\cdot\boldsymbol{\sigma}=\boldsymbol{\nabla}\cdot\boldsymbol{T}_{\mathrm{m}} \quad \text{in } \Omega, \tag{11}$$

$$\boldsymbol{\nabla}\cdot\boldsymbol{u}=0 \quad \text{in } \Omega, \tag{12}$$

$$\boldsymbol{\sigma}=-p\boldsymbol{I}+2\eta\boldsymbol{D} \quad \text{in } \Omega, \tag{13}$$

$$\boldsymbol{u}=\boldsymbol{U}_i+\boldsymbol{\omega}_i\times\boldsymbol{r}_i \quad \text{on } \partial P_i(t) \quad (i=1,\ldots,N), \tag{14}$$

$$\boldsymbol{u}=\boldsymbol{0} \quad \text{on } \Gamma_w, \tag{15}$$

where $\boldsymbol{\sigma}$ is the Cauchy stress tensor, $\boldsymbol{T}_{\mathrm{m}}$ the Maxwell stress tensor, $\boldsymbol{u}$ the velocity, p the pressure, η the viscosity, $\boldsymbol{D}$ the rate-of-deformation tensor, $\boldsymbol{U}_i$ the translational velocity of the ith particle, $\boldsymbol{\omega}_i$ the angular velocity of the ith particle, and $\boldsymbol{r}_i=\boldsymbol{x}-\boldsymbol{X}_i$ with $\boldsymbol{x}$ the position vector of a point on the ith particle boundary ∂P_i, and $\boldsymbol{X}_i$ the position vector of the center of the ith particle. Equations (11)–(13) are the momentum balance equation, the continuity equation, and the constitutive relation for the fluid domain, respectively. Equations (14) and (15) are the constraints for rigid-body motion of the particles and the essential boundary condition at the solid wall, respectively.

In addition to the above-mentioned governing equations, boundary conditions, and constraints, one needs to solve the kinematic equations for the evolution of particle positions with time t, represented by

$$\frac{d\boldsymbol{X}_i}{dt}=\boldsymbol{U}_i, \quad \boldsymbol{X}_i(0)=\boldsymbol{X}_{i,0}, \tag{16}$$

$$\frac{d\boldsymbol{\Theta}_i}{dt}=\boldsymbol{\omega}_i, \quad \boldsymbol{\Theta}_i(0)=\boldsymbol{\Theta}_{i,0}. \tag{17}$$

Finally, balance equations are needed for the drag force and torque on particles to determine the unknown rigid-body motions $(\boldsymbol{U}_i,\boldsymbol{\omega}_i)$ of the particles. In the absence of inertia, the balance equations are represented as follows:

$$\boldsymbol{F}_i=\int_{\partial P_i^+(t)}(\boldsymbol{\sigma}+\boldsymbol{T}_m)\cdot\boldsymbol{n}\,dS=\boldsymbol{0}, \tag{18}$$

$$\boldsymbol{T}_i=\int_{\partial P_i^+(t)}\boldsymbol{r}_i\times[(\boldsymbol{\sigma}+\boldsymbol{T}_m)\cdot\boldsymbol{n}]dS=\boldsymbol{0}, \tag{19}$$

where $\boldsymbol{F}_i$ is the sum of the hydrodynamic drag and magnetic force, $\boldsymbol{T}_i$ is the sum of the hydrodynamic torque and magnetic torque working on a rigid particle, and $\boldsymbol{n}$ the outward normal vector at the particle boundary.

III. NUMERICAL METHODS

A. Magnetic problem

The weak form of the Poisson equation (6) for the magnetic potential A is given as follows: find $A\in\mathbb{S}$ such that

$$\int_\Omega\frac{1}{\mu_r}(\boldsymbol{\nabla}A\cdot\boldsymbol{\nabla}\psi)dA=\int_\Omega\mu_0 J\,dA, \tag{20}$$

for all $\psi\in\mathbb{S}_0$ with $\mathbb{S}=\{A\in H^1(\Omega)$ with $A=\bar{A}$ at $\Gamma_w\}$ and $\mathbb{S}_0=\{\psi\in H^1(\Omega)$ with $\psi=0$ at $\Gamma_w\}$. The continuity of A, Eq. (9), holds in the standard finite-element formulation. The continuity of the tangential component of $\boldsymbol{H}$, which is represented by the continuity of flux in the diffusion equation of the magnetic potential A, Eq. (10), is weakly satisfied in the finite-element formulation. The weak form is used to obtain an approximate solution using the finite-element method with biquadratic interpolation for A. The resulting matrix equation is solved using a sparse Gauss elimination method, HSL/MA57 [20], to solve a symmetric matrix.

B. Flow problem

The fluid flow problem, including interactions between fluid and rigid particles, is solved by using a fictitious domain method and the finite-element method. We use a fictitious domain method to treat rigid-body constraints on particle boundaries. In the derivation of the weak form, following the approach of [21], fluid-particle interactions are implicitly treated through the combined weak formulation, where the hydrodynamic force and torque on the particle boundaries are canceled exactly. In the combined weak for-

mulation, the rigid-body constraint is enforced by the constraint equation using a Lagrange multiplier $\boldsymbol{\lambda}^{\mathrm{p},i}$ defined on the particle boundary ∂P_i.

Let us first define the combined velocity and variational space for the velocity, which is denoted by $\mathbb{V}$:

$$\mathbb{V} = \{ (\boldsymbol{u}, \boldsymbol{U}_i, \boldsymbol{\omega}_i) | \boldsymbol{u} \in H^1(\Omega)^2, \ \boldsymbol{U}_i \in \mathbb{R}^2, \ \boldsymbol{\omega}_i \in \mathbb{R}, \ \boldsymbol{u} = \boldsymbol{U}_i + \boldsymbol{\omega}_i \times \boldsymbol{r}_i \ \text{on} \ \partial P_i(t) \ \text{and} \ \boldsymbol{u} = \boldsymbol{0} \ \text{on} \ \Gamma_w \} \tag{21}$$

for $i=1,\ldots,N$. For a given particle configuration $\boldsymbol{X}_i$ $(i=1,\ldots,N)$, the weak form for the entire domain Ω can be stated as follows: find $(\boldsymbol{u}, \boldsymbol{U}_i, \boldsymbol{\omega}_i) \in \mathbb{V}$, $p \in L^2(\Omega)$, and $\boldsymbol{\lambda}^{\mathrm{p},i} \in \mathbf{L}^2(\partial P_i(t))$ $(i=1,\ldots,N)$ such that

$$\int_\Omega 2\eta \boldsymbol{D}(\boldsymbol{v}):\boldsymbol{D}(\boldsymbol{u}) dA - \int_\Omega (\boldsymbol{\nabla}\cdot\boldsymbol{v}) p \, dA + \sum_{i=1}^{N} \langle \boldsymbol{v} - (\boldsymbol{V}_i + \boldsymbol{\chi}_i \times \boldsymbol{r}_i), \boldsymbol{\lambda}^{\mathrm{p},i} \rangle_{\partial P_i} = -\int_\Omega \boldsymbol{D}(\boldsymbol{v}):\boldsymbol{T}_{\mathrm{m}} dA, \tag{22}$$

$$-\int_\Omega q(\boldsymbol{\nabla}\cdot\boldsymbol{u}) dA = 0, \tag{23}$$

$$\langle \boldsymbol{\mu}^{\mathrm{p},i}(\boldsymbol{x}), \boldsymbol{u}(\boldsymbol{x}) - (\boldsymbol{U}_i + \boldsymbol{\omega}_i \times \boldsymbol{r}_i) \rangle_{\partial P_i} = 0, \tag{24}$$

for all $(\boldsymbol{v}, \boldsymbol{V}_i, \boldsymbol{\chi}_i) \in \mathbb{V}$, $q \in L^2(\Omega)$, and $\boldsymbol{\mu}^{\mathrm{p},i} \in \mathbf{L}^2(\partial P_i(t))$ $(i=1,\ldots,N)$. In the weak formulation, instead of using the divergence of the Maxwell stress tensor as it is, we applied integration by part and the Gauss theorem. This form allows us to circumvent differentiation of the Maxwell stress tensor, which is discontinuous at fluid-particle interfaces. We use biquadratic interpolation for the velocity and bilinear interpolation for the pressure, the so-called Q_2/Q_1 element. As for the rigid-body constraints, the weak form is approximated by point collocation [17]. The resulting matrix equation is solved by the same direct sparse matrix solver as used in the magnetic problem.

Particle positions are updated by integrating the evolution equations (16), using the rigid-body motions of the particles obtained as a part of the solution. We employ explicit time integration schemes. The explicit Euler method [Eq. (25)] is used at the first time step and the second-order Adams-Bashforth method [Eq. (26)] from the second time step onwards:

$$\boldsymbol{X}_i^{n+1} = \boldsymbol{X}_i^n + \Delta t \boldsymbol{U}_i^n, \tag{25}$$

$$\boldsymbol{X}_i^{n+1} = \boldsymbol{X}_i^n + \Delta t \left(\frac{3}{2}\boldsymbol{U}_i^n - \frac{1}{2}\boldsymbol{U}_i^{n-1} \right), \tag{26}$$

where variables with superscripts $n-1$, n, and $n+1$ represent those evaluated at the previous time, the present time, and the next time step, respectively.

C. Remarks

We employ a direct numerical scheme [16] taking into account both hydrodynamic and magnetic interactions in a coupled manner, using a fictitious domain method and the Maxwell stress tensor formulation. The dipole-dipole interaction model used by other authors [12,15] is quite effective if the length scale of the field nonuniformity is much larger than the particle size [22,23]. However, this assumption may be violated in microfluidic applications because practical sources of magnetic fields—for example, permanent magnets or current-carrying wires—become smaller with miniaturization, leading to a decrease in the length scale of the field nonuniformity as well. Therefore, in applications with the particle size comparable to the length scale of the field nonuniformity, due to closely spaced particles or particles close to a magnetic source, the present approach is more favorable than that based on the dipole moment method. In addition, the present scheme has several advantages from the viewpoint of implementation: (i) easy implementation in a code based on the finite-element method, regardless of the shape of particles, (ii) easy treatment of inhomogeneous magnetic permeability, possibly also depending on the magnetic field intensity, and (iii) direct simulation of particulate flows with both hydrodynamic and magnetic interactions. Finally, in this work, we did not employ an artificial particle-particle collision scheme by choosing a relatively small time step in a sufficiently refined mesh. In the problems introduced, the particle overlap could be avoided or minimized to a negligible extent, even in problems involving chain breakup and reformation, which will be introduced shortly.

IV. RESULTS AND DISCUSSION

We first introduce the result of a scaling analysis for the momentum balance equation (11), aiming to extract nondimensional parameters influencing the dynamics of the chain and the subsequent fluid flow. Next introduced are the dynamics of a magnetic chain, flow characteristics, interface tracking, and mixing analysis at several Mason numbers [see Eq. (32)], ranging from 0.0005 to 0.05, in which we observe three regimes of Mason number with distinct dynamics of the chain and flow characteristics. In the simulations, we use a fixed value of the magnetic susceptibility of the particles, $\chi_{\mathrm{p}}=1$,[1] and assumed that there is no current source, i.e., $J=0$. The ratio of particle radius to cavity radius is $a/R_c=0.05$, so the area fraction of the particles equals 0.0425 with the number of particles, $N=17$. The circular cavity is discretized into 14 400 nine-node quadrilateral elements. The number of collocation points describing the particle boundary is determined such that there are approximately two collocation points per element, based on previous numerical experiments [16]. The time period of the rotating magnetic field is 2π in dimensionless time. The time step is 0.02 in nondimensional units.

[1] We use a typical value of the magnetic susceptibility χ_{p} for commercially available magnetic beads—for example, polystyrene beads with dispersed superparamagnetic nanoparticles [6,7].

A. Scaling analysis

Nondimensional variables (with a superscript *) are given by

$$x^* = \frac{x}{l_c}, \quad y^* = \frac{y}{l_c}, \tag{27}$$

$$\boldsymbol{u}^* = \frac{\boldsymbol{u}}{u_c}, \tag{28}$$

$$p^* = \frac{p}{p_c}, \tag{29}$$

$$T_{ij}^* = \frac{T_{ij} - \mu_0 H_c^2}{(\mu_p - \mu_0) H_c^2}, \tag{30}$$

where l_c denotes a characteristic length, $\boldsymbol{u}_c$ a characteristic velocity, p_c a characteristic pressure, and H_c the characteristic magnetic field intensity. Here, we define the characteristic length as a particle radius, $l_c = a$. The characteristic time is defined as the inverse of the angular frequency of the magnetic field, $t_c = \omega^{-1}$—thus, $t^* = \omega t$. Then, the characteristic velocity and pressure are defined as $u_c = a/t_c = a\omega$ and $p_c = \eta u_c / a = \eta\omega$, respectively. The Maxwell stress tensor T_{ij} is nondimensionalized by the stress difference (with the reference being $\mu_0 H_c^2$) normalized by $(\mu_p - \mu_0) H_c^2$. The characteristic magnetic field intensity is defined as $H_c = H_0 = B_0/\mu_0$. Then, the resulting nondimensional momentum equation becomes

$$\boldsymbol{\nabla}^* p^* - \nabla^{*2} \boldsymbol{u}^* = \frac{1}{\mathrm{Ma}} \boldsymbol{\nabla}^* \cdot \boldsymbol{T}^*. \tag{31}$$

In Eq. (31), Ma is the Mason number,[2] which is the ratio of viscous force to magnetic force under the influence of a rotating magnetic field, defined by

$$\mathrm{Ma} = \frac{\eta\omega}{\mu_0 \chi_p H_0^2}, \tag{32}$$

with χ_p being the magnetic susceptibility of the particles, $\chi_p = \mu_{rp} - 1$. The magnetic permeability χ_p is also one of the parameters governing the dynamics of the chain, which in this study is assumed to be constant. In this paper, therefore, the Mason number used is defined for other parameters such as the magnetic permeability, the ratio of particle size to cavity size, and the area fraction of the particles being fixed.

At a lower Mason number magnetic forces are dominant, while at a higher Mason number viscous forces are dominant. With such parameters as the susceptibility of particles, the particle area fraction, and the ratio of particle size to cavity size being fixed, the Mason number is a key parameter determining the dynamics of the chain and the characteristics of the flow induced in a rotating magnetic field. In simulations introduced in the following sections, we focus on the effect of the Mason number on the chain motion, fluid flow, and mixing.

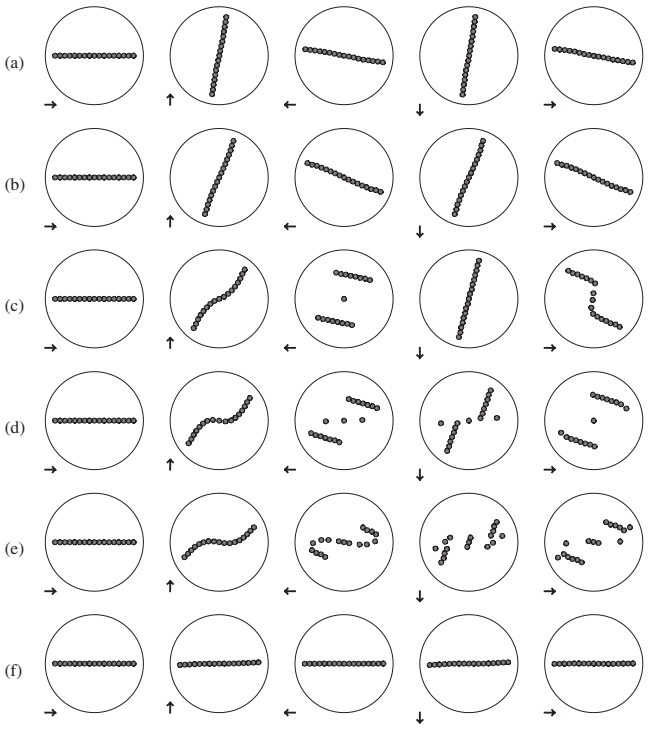

FIG. 2. Dynamics of the chain at the six Mason numbers (a) Ma=0.0005, (b) Ma=0.001, (c) Ma=0.002, (d) Ma=0.003, (e) Ma=0.005, and (f) Ma=0.05. The shapes of the chain are plotted at the nondimensional time $t^*=0$, $\frac{1}{2}\pi$, π, $\frac{3}{2}\pi$, and 2π (from left to right). Here, the nondimensional time is defined as $t^*=\omega t$ and the time period of the rotating field is 2π. The arrows indicate the direction of the magnetic field.

B. Chain dynamics

Figure 2 depicts a series of deformation patterns of the chain at six Mason numbers Ma=0.0005, 0.001, 0.002, 0.003, 0.005, and 0.05, illustrating that the dynamics of the chain is significantly dependent on the Mason number. The arrows in the figures indicate the direction of the applied magnetic field at a certain nondimensional time.

At the two lower Mason numbers Ma=0.0005 and 0.001, the chain rotates almost like a rigid chain following the rotating field, but lags behind the field [see Figs. 2(a) and 2(b)]. Here, we observe an increased phase lag with the Mason number. As the Mason number increases further, due to the increased viscous drag and magnetic interactions among the particles, chain breakup is observed at the three intermediate Mason numbers Ma=0.002, 0.003, and 0.005. At Ma =0.002, the chain is split into two chains, connecting again to form a single chain, which takes places in an alternating

[2]The derived Mason number, Eq. (32), has a different form from those found in the literature [12–15], with different proportionality factors. The typical value of Ma, showing a transition in chain dynamics, is $O(10^{-3})$ in our flow problems. Higher values for the Mason number may result from the use of a characteristic velocity $u_c = Na\omega$ rather than $u_c = a\omega$ as used here. The value of the critical Mason number showing transition may vary with a change of the parameters χ_p, a/R, and N.

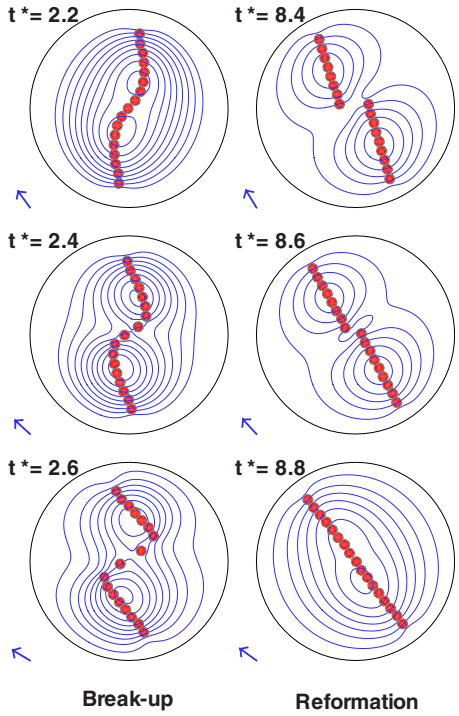

FIG. 3. (Color online) Streamlines and chain configurations at the moment of chain breakup (left) and reformation (right) at Ma =0.002. At chain breakup, hyperbolic flow is clearly observed and the deformed chain reveals a reverse S-like structure.

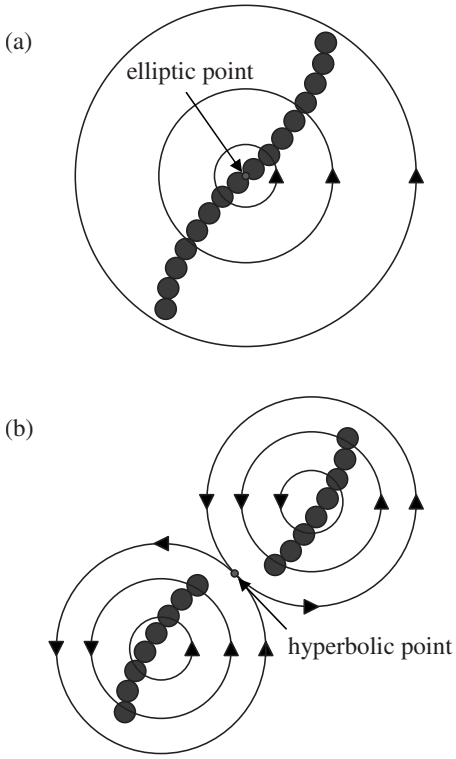

FIG. 4. Two typical flow portraits induced by the topological changes of the chain at Ma=0.002: (a) one rotating flow with an elliptic point and (b) two corotating flows with two elliptic points and one hyperbolic point.

manner [see Fig. 2(c)]. Especially, the shape of chain at the moment of breakup, a reversed S-like structure, is quite similar to that observed experimentally by [13] (see also Fig. 3 for detailed deformation patterns at breakup). At Ma=0.003, as shown in Fig. 2(d), the chain is broken into two chains as well, but the two detached chains remain as separate chains without joining together. In the third case, at Ma=0.005, the chain is now folded and split into three chains and some single particles, which also remain as separate chains [see Fig. 2(e)]. At an even higher Mason number Ma=0.05, the chain behaves like a rigid body again, but on average, the chain rotates with a frequency much lower than that of the rotating field. On top of that, it oscillates with a frequency close to that of the rotating field.

In summary, the dynamics of the chain is significantly influenced by the Mason number and three distinct regimes with different chain dynamics can be distinguished. At a lower Mason number, the chain rotates following the field with a phase lag, and the larger the Mason number, the higher the phase lag. In the intermediate regime, with the Mason number ranging from 0.002 to 0.01, chain breakup is observed, with the number of detached chains increasing with Mason number. In the third regime, where the Mason number is higher than 0.01, the chain behaves as a rigid chain again. The chain rotates in an overall sense, with an additional oscillatory motion.

C. Flow characteristics

Now, we move our attention to flow characteristics induced by the chain motion and, especially, to chaotic advection characterized by a spatial distribution of maximum Lyapunov exponents. As a representative example, detailed flow characteristics in the most interesting case of Ma =0.002 will be discussed.

Figure 3 shows streamlines at the moment of breakup and reformation of the chain at Ma=0.002. The flow induced by the motion of the chain is characterized by two typical flow portraits: a single rotating flow with one elliptic point and two corotating flows with one hyperbolic point and two elliptic points, as schematically illustrated in Fig. 4. The two flows have the following characteristics: (i) overall rotational motion induced by the rotation of the chain and (ii) hyperbolic flow around the point of chain breakup, leading to a large stretching of the fluid. In addition, the repetition of the two flow portraits is known as an efficient way of inducing chaotic mixing in macromixing and micromixing devices [24,25]. Therefore, the alternation of these two types of flows may be a good mixing protocol to achieve enhanced mixing via chaotic advection induced by the flow with a magnetic chain. At higher Mason numbers Ma=0.003, 0.004, and 0.005, the detached chains induce only two, three, or more corotating flows, which we expect to be less effective as a mixing protocol than the two alternating flows at Ma =0.002.

Therefore, next we need to find out at which Mason number the flow creates more chaotic trajectories of fluid particles, which in turn results in better mixing. One of the manifestations of chaos related to mixing is the sensitivity to initial conditions determined by flow characteristics. A rapid

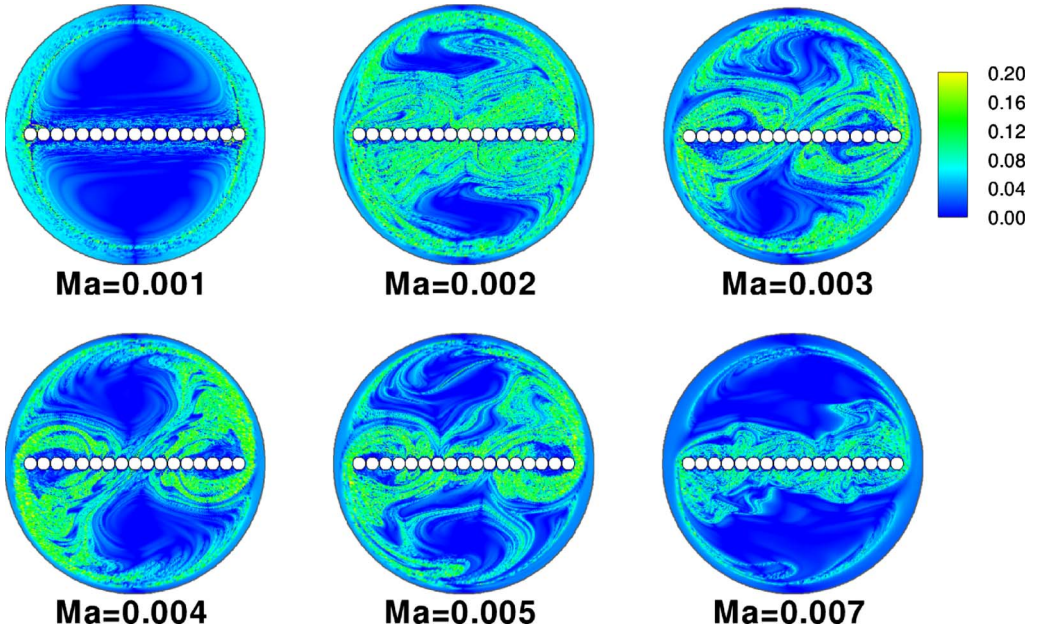

FIG. 5. (Color online) Spatial distributions of the maximum Lyapunov exponent σ at several Mason numbers Ma=0.001, 0.002, 0.003, 0.004, 0.005, and 0.007.

divergence of initial conditions is a signature of chaotic system, which is usually quantified by means of Lyapunov exponents [5,26]. Dynamical systems with n degrees of freedom have n different Lyapunov exponents σ_i $(i=1,\ldots,n)$,

$$\sigma_i(\boldsymbol{Y},\boldsymbol{M}_i) = \lim_{\substack{x\to\infty \\ |d\boldsymbol{Y}|\to 0}} \left[\frac{1}{t}\ln\left(\frac{|d\boldsymbol{y}|}{|d\boldsymbol{Y}|}\right)\right], \tag{33}$$

where $d\boldsymbol{Y}$ represents an infinitesimal fluid element vector with an initial orientation $\boldsymbol{M}_i = d\boldsymbol{Y}/|d\boldsymbol{Y}|$ and $d\boldsymbol{y}$ the vector at time t. The presence of a positive Lyapunov exponent is a signature of chaos in a flow system, showing an exponential divergence of two neighboring particle orbits initially separated by an infinitesimally small distance. To find the maximum Lyapunov exponent σ, we employ a numerical scheme proposed by [26], given by

$$\sigma = \lim_{K\to\infty} \frac{1}{K\Delta t}\sum_{k=1}^{K} \ln\left[\frac{dy(k)}{dy(0)}\right], \tag{34}$$

where Δt is the time step and $dy(0)$ the initial separation between two passive tracers in flow and $dy(k)$ the separation between the two tracers after k time steps. The idea in this scheme is to follow two nearby orbits and to calculate their average logarithmic rate of separation.

We calculated Lyapunov exponents using velocity solutions obtained at six Mason numbers Ma=0.001, 0.002, 0.003, 0.004, 0.005, and 0.007. In all cases, calculations are conducted to the finite time corresponding to approximately 12 rotations of the magnetic field, with the initial distance between two nearby orbits $dy(0)=10^{-12}$. Figure 5 depicts the spatial distributions of maximum Lyapunov exponents in the cavity at the six Mason numbers. The larger the area with positive exponent, the larger chaotic region in the domain. To quantitatively measure the degree of chaos, the area fraction $\alpha = A_c/A$ is plotted as a function of Mason number (see Fig. 6). Here, A_c is the area of the region with the Lyapunov exponent larger than a cutoff value σ_c, i.e., $A_c = A|_{\sigma>\sigma_c}$, and A is the area of the whole domain.

From Fig. 6, one can find an optimal Mason number at which a flow system is the most chaotic. In the case of the problem investigated, the optimal Mason number is indeed found around Ma=0.002, where breakup and reformation of the chain are taking place alternatingly as shown in Fig. 3. Therefore, we can expect that mixing at this Mason number will also be better than at the other Mason numbers, which will be verified both qualitatively and quantitatively in the

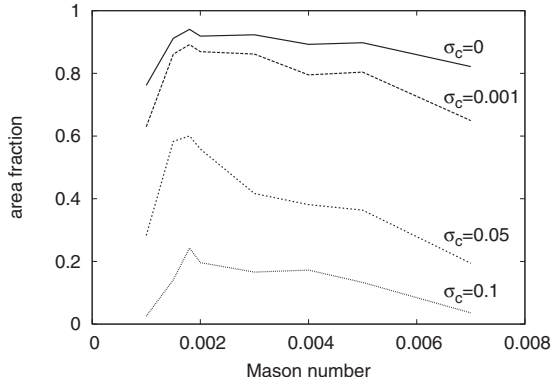

FIG. 6. Area fraction (α) of the region with the Lyapunov exponent larger than a cutoff value σ_c, defined by $\alpha = A|_{\sigma>\sigma_c}/A$, where A is the area of the whole domain and $A|_{\sigma>\sigma_c}$ the area with $\sigma > \sigma_c$. At a Mason number around 0.002, the chaotic region is the largest, indicating the existence of an optimal Mason number yielding efficient chaotic mixing.

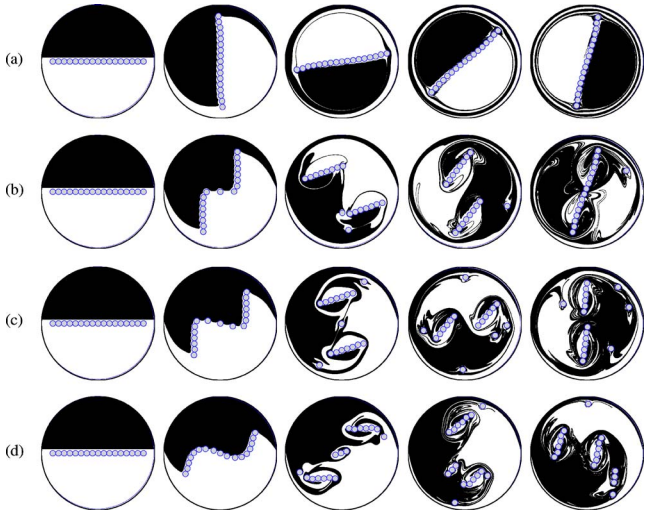

FIG. 7. (Color online) Deformation of the interface between "black" and "white" fluids for the four Mason numbers (a) Ma =0.001, (b) Ma=0.002, (c) Ma=0.003, and (d) Ma=0.005. The evolution of the deforming interface is plotted at the nondimensional time t^*=0, 2, 10, 20, and 30 (from left).

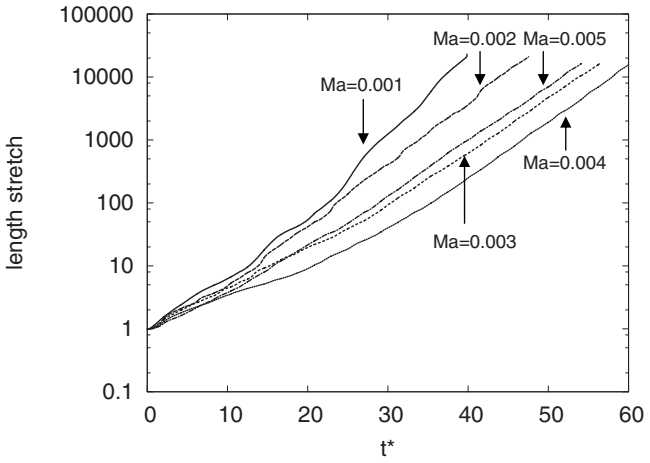

FIG. 8. Evolution of the length stretch λ of the interface for the five Mason numbers Ma=0.001, 0.002, 0.003, 0.004, and 0.005. Here, the length stretch is defined as $\lambda = l(t^*)/l_0$, where $l(t^*)$ and l_0 denote the interfacial length at time t^* and at the initial state, respectively.

next two sections via interface tracking and colored tracer tracking.

D. Interface tracking

The increase in the interfacial surface area (or interfacial length in the 2D case) may be a measure of mixing for mixtures without diffusion. In this section, we track the interface between "black" and "white" fluids (see Fig. 7) in time, attempting to investigate in-depth deformation patterns of fluid elements and to characterize the increase of interfacial length. Here, we are mainly concerned with the kinematics of fluid motion. An adaptive front-tracking method [27] is employed to precisely track interfaces undergoing complicated deformation patterns. This method makes it possible to track interfaces that experience an exponential increase in length due to chaotic advection, accurately preserving the area.

Figure 7 shows the evolution of the interface at four Mason numbers Ma=0.001, 0.002, 0.003, and 0.005, with the initial configuration illustrated in the first column. As expected from the Lyapunov exponent shown in Fig. 5, the evolution of the interface is affected by the Mason number. From the deformation patterns, we clearly see how the fluid deforms with flow. A large stretching of fluid elements is observed near the tips of the rotating chains and at the points of chain breakup, and the stretched fluid elements are folded by the rotational flows. The detailed mechanism of stretching and folding generated by the chain motion is dependent on the Mason number.

The increase of the interfacial length is characterized by the length stretch of the fluid elements, as shown in Fig. 8. The length stretch λ is defined as $\lambda = l(t^*)/l_0$, where $l(t^*)$ is the interfacial length at time t^* and l_0 is the initial interfacial length. The length stretch shows an exponential growth in all the cases. Although the largest stretching is found at Ma =0.001, stretching is constrained to a narrow ring between the cavity wall and both ends of the chain and, consequently, mixing is poor [see Fig. 7(a)]. For most applications, not only the total amount of interfluid interfaces is important, but also their spatial distribution in the bulk of the fluid. Apparently, the length stretch as such is not a proper measure of mixing quality, as was already concluded by [28] in optimization of the Kenics static mixer. The exponential length stretch at Ma=0.002 originates from stretching and folding induced by the alternating topological changes of the chain. From the deformation patterns in Fig. 7 and the spatial distributions of the maximum Lyapunov exponents in Fig. 5, one can expect that flows induced by breakup and reformation of the chain are better for mixing than those by a singe chain, which will be discussed in the following section.

E. Mixing analysis

In the absence of precise periodicity in these flows, the mapping method [29], as successfully applied in optimizing different mixers, cannot be used. Progress of mixing can, however, also be visualized using a tracer-tracking method [30], yielding also both qualitative and quantitative measures for mixing. In the beginning, a number of passive tracer particles, labeled with either red or blue indicating the species of a fluid, are uniformly introduced in the entire domain. Then, the positions of all tracer particles are tracked using the transient velocity field stored at each time step. Tracking of individual tracer particles is accomplished using a fourth-order Runge-Kutta method to the time one wants to analyze. The essence of this stage is the colors labeled to the tracers according to their species, resulting in the distribution of colored tracers at a time t^*. The obtained color patterns of the tracers provide the intrinsic information on a certain mixing state, on which a mixing measure will be based. In what follows, we first introduce the measure of mixing and then show the results.

We employ a measure of mixing based on the intensity of segregation. In general, the intensity of segregation is a measure of the deviation of the local concentration from the ideal situation of a homogeneous state of the mixture, defined as the second-moment variance of the concentration distribution:

$$I = \frac{\sigma_c^2}{\bar{c}(1-\bar{c})}, \tag{35}$$

where σ_c^2 is the variance in the concentration over entire domain Ω defined as

$$\sigma_c^2 = \langle (c(\boldsymbol{x}) - \bar{c})^2 \rangle_\Omega, \tag{36}$$

where $c(\boldsymbol{x})$ denotes the concentration at a point $\boldsymbol{x}$ and $\bar{c}$ the average concentration in the domain. The denominator of Eq. (35) is defined such that the value of I always varies from unity to zero with the progress of mixing. In a perfectly mixed system, $I=0$, while in a completely unmixed system, $I=1$. For more details on the definition, we refer to the original work by [31].

In this study, we define the concentration in a subdomain, based on the tracer distribution and use a discrete version of I, called the discrete intensity of segregation I_d, as a measure of mixing. For that purpose, we divide the cavity domain into M cells (subdomains), which differ from the finite-element mesh, and count the number of red and blue tracers at all cells constituting the cavity. Then, from a given tracer distribution, we define the concentration of blue tracer C_i in the ith cell, and the average concentration $\bar{C}$, as follows:

$$C_i = \frac{n_i^b}{n_i}, \tag{37}$$

$$\bar{C} = \sum_{i=1}^{M} f_i C_i, \tag{38}$$

where n_i denotes the sum of red and blue tracers in the cell, $n_i = n_i^r + n_i^b$, with n_i^r and n_i^b being the number of red and blue tracers in the cell, respectively, and f_i is the tracer number fraction, $f_i = n_i / \Sigma n_i$, used as a weighting factor in averaging. Finally, the discrete intensity of segregation I_d is calculated using

$$I_d = \frac{1}{\bar{C}(1-\bar{C})} \sum_{i=1}^{M} f_i (C_i - \bar{C})^2, \tag{39}$$

which is a normalized variance in the concentration C_i. The cavity is divided into 2300 cells, i.e., $M=2300$. We initially introduce about 100 000 passive tracer particles with the same number of red and blue tracers. Two initial configurations, in which the interface of the two fluids is either vertical or horizontal to the magnetic chain, initially aligned horizontally, are chosen as two extreme cases. Each tracer has an intrinsic property, an indicator of the species of fluid (in this study represented by color), together with its position in time. Therefore, an initial configuration of tracers reflects the initial condition of two fluids before mixing. The evolution of colored tracers can qualitatively depict mixing of two species and is used as a basis for the quantification of mixing.

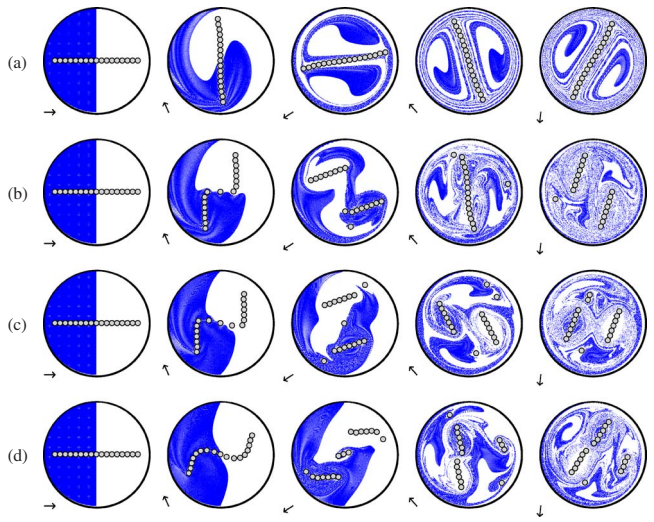

FIG. 9. (Color online) Progress of mixing visualized via a colored tracer tracking at the nondimensional time $t^*=0$, 2, 10, 40, and 80 (from left) for the four Mason numbers (a) Ma=0.001, (b) Ma=0.002, (c) Ma=0.003, and (d) Ma=0.005. Although all the tracer particles with either red or blue color were tracked to the nondimensional time $t^*=80$, for clarity, only the evolution of blue tracers is shown. Initially, the interface between two fluids is perpendicular to the chain, which is a more favorable initial configuration for mixing, compared with the case with a horizontal interface as shown in Fig. 10.

Figures 9 and 10 show the evolution of the tracers for the four Mason numbers Ma=0.001, 0.002, 0.003, and 0.005 [32]. For clarity of visualization, only blue tracers are shown in the figures. An instantaneous distribution of the tracers qualitatively reflects a mixing state and is used as a basis for the quantification of mixing. At Ma=0.001, as depicted in

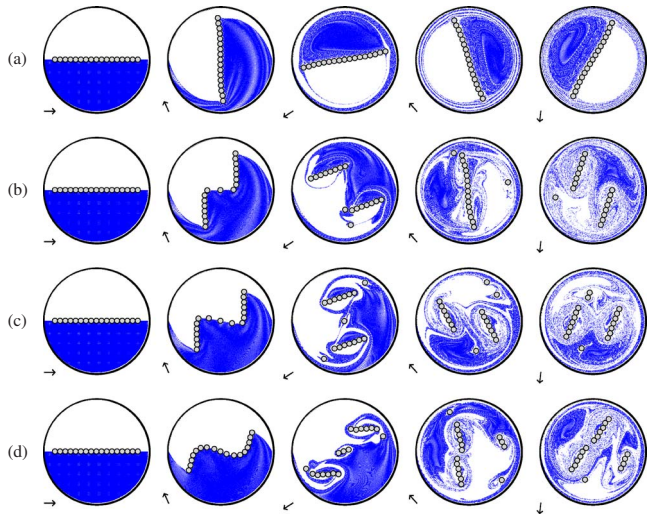

FIG. 10. (Color online) Progress of mixing visualized via a colored tracer tracking at the nondimensional time $t^*=0$, 2, 10, 40, and 80 (from left) at the four Mason numbers (a) Ma=0.001, (b) Ma=0.002, (c) Ma=0.003, and (d) Ma=0.005. Initially, the interface of the two fluids is aligned with the chain.

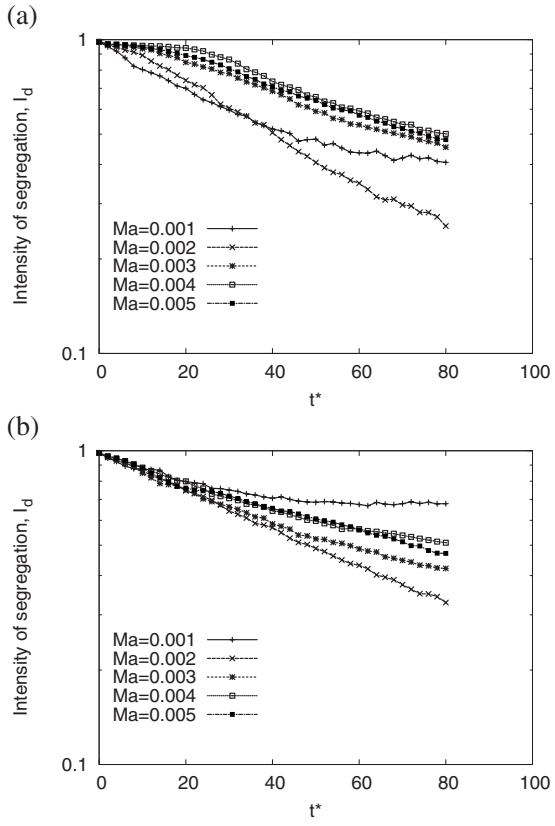

FIG. 11. Discrete intensity of segregation I_d with time for the two different initial configurations of the two fluids labeled with red or blue: (a) vertical interface (Fig. 9) and (b) horizontal interface (Fig. 10). Note that smaller I_d corresponds to better mixing.

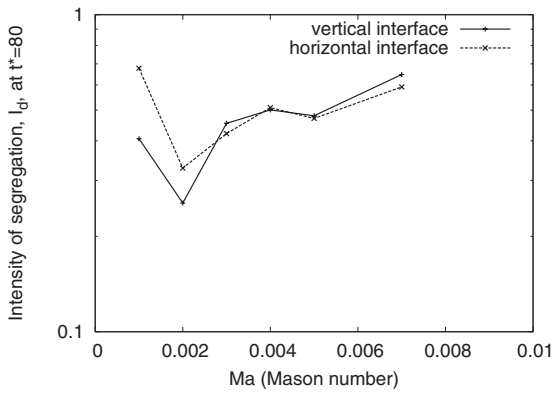

FIG. 12. Discrete intensity of segregation I_d at $t^*=80$ vs the Mason number for the two different initial configurations of the two fluids, forming either vertical or horizontal interface. An optimal Mason number exists near Ma=0.002 in the sense of minimizing I_d.

Fig. 9(a), we observe mixing to some degree, around the chain and rim of the cavity. In the case of the coincident interface with the chain [see Fig. 10(a)], however, mixing is poor because of the chain acting as a barrier preventing the two fluids from moving across. At the other Mason numbers, where chain breakup is observed, mixing is less affected by the initial configuration of the interface of the fluids. Figure 11 plots the discrete intensity of segregation I_d as a function of time t^*. For the given initial configuration of the tracers, the mixing rate and the final mixing state, measured by I_d, are significantly influenced by the Mason number and also affected by the initial configuration of the two fluids. According to the tracer distributions and plots of the discrete intensity of segregation, mixing at Ma=0.002 is the best, regardless of the initial configuration of the interface of the two fluids. From the discrete intensity of segregation at $t^*=80$ as a function of the Mason number (see Fig. 12), we conclude that there is a limited range of Mason numbers, for which efficient mixing can be achieved.

V. CONCLUSION

The use of magnetic chains, formed by magnetic particles, as active microstirrers, has attractive applications in future diagnostic lab-on-a-chip devices. We carried out a fundamental study on chaotic mixing induced by a magnetic chain in the presence of a rotating magnetic field, concentrating on the dynamics of the chain, the characteristics of the flow induced, and the route to chaotic mixing. A direct simulation method based on the Maxwell stress tensor and a fictitious domain method has been utilized to solve flows with a suspended magnetic chain in a two-dimensional circular cavity. The numerical method enables us to take into account both hydrodynamic and magnetic interactions in a fully coupled manner. The motion of the chain, fluid flow, and mixing are significantly influenced by the Mason number, the ratio of viscous force to magnetic force.

We observe three regimes of Mason number with distinct dynamics of the chain. At a lower Mason number, the chain behaves like a rigid body; thus, it rotates as a single chain following the field, but lags behind the field. In the intermediate Mason numbers, where $0.001<\mathrm{Ma}<0.01$, chain breakup is observed with the number of detached chains increasing with the Mason number. At the Mason number around Ma=0.002, the two split chains rejoin together, forming a single chain again, and this splitting and reconnecting takes place in an alternating manner. At Mason numbers higher than 0.002 and less than 0.01, the split chains remain separate without connecting again. In the third regime, where $\mathrm{Ma}\geq 0.01$, we observe a rigid-chain behavior again. The chain rotates in an overall sense, with an extra oscillatory motion superposed. The alternating breakup and reformation of the chain at Ma=0.002 creates two typical flows: one rotating flow and two corotating flows. The two repeating flows result in the largest chaotic region, characterized by the maximum Lyapunov exponent, and induce an exponential increase of the interfacial length. The progress of mixing is visualized via a colored-tracer particle-tracking method. Using the discrete intensity of segregation based on the distribution of the tracers, we quantitatively characterized the progress of mixing, dependent on the Mason number and also on the initial configuration of the two fluids to be mixed. From the results of the mixing analysis, the alternating topological changes of the chain, breakup and reformation, turned out to be the key mechanism of chaotic mixing, which lead to stretching at chain breakup and folding by the rotational flows, and therefore an optimal Mason number exists

around Ma=0.002.

In addition to the Mason number, other parameters such as the magnetic permeability of the particles, particle size, cavity geometry, and frequency modulation of a rotating magnetic field have significant influences on the chain motion. These are subject of future study as well as the influence of non-Newtonian fluids on the chain dynamics, fluid flow, and subsequent mixing.

[1] D. R. Reyes, D. Iossifidis, P. A. Auroux, and A. Manz, Anal. Chem. **74**, 2623 (2002).

[2] T. M. Squires and S. R. Quake, Rev. Mod. Phys. **77**, 977 (2005).

[3] A. D. Stroock, S. K. Dertinger, A. Ajdari, I. Mezic, H. A. Stone, and G. M. Whitesides, Science **295**, 647 (2002).

[4] H. Aref, J. Fluid Mech. **143**, 1 (1984).

[5] J. M. Ottino, *The Kinematics of Mixing: Stretching, Chaos, and Transport* (Cambridge University Press, Cambridge, England, 1989).

[6] M. A. M. Gijs, Microfluid. Nanofluid. **1**, 22 (2004).

[7] N. Pamme, Lab Chip **6**, 24 (2006).

[8] N. Pamme and A. Manz, Anal. Chem. **76**, 7250 (2004).

[9] A. Rida and M. A. M. Gijs, Anal. Chem. **76**, 6239 (2004).

[10] H. Suzuki, C.-M. Ho, and N. Kasagi, J. Microelectromech. Syst. **13**, 779 (2004).

[11] S. Melle, G. G. Fuller, and M. A. Rubio, Phys. Rev. E **61**, 4111 (2000).

[12] S. Melle and J. E. Martin, J. Chem. Phys. **118**, 9875 (2003).

[13] S. Melle, O. G. Calderon, M. A. Rubio, and G. G. Fuller, Phys. Rev. E **68**, 041503 (2003).

[14] S. L. Biswal and A. P. Gast, Phys. Rev. E **69**, 041406 (2004).

[15] R. Calhoun, A. Yadav, P. Phelan, A. Vuppu, A. Garciab, and M. Hayes, Lab Chip **6**, 247 (2006).

[16] T. G. Kang, M. A. Hulsen, J. M. J. den Toonder, P. D. Anderson, and H. E. H. Meijer (unpublished).

[17] W. R. Hwang, M. A. Hulsen, and H. E. H. Meijer, J. Comput. Phys. **194**, 742 (2004).

[18] J. A. Stratton, *Electromagnetic Theory* (McGraw-Hill, New York, 1941).

[19] C. Rinaldi and H. Brenner, Phys. Rev. E **65**, 036615 (2002).

[20] HSL, a collection of FORTRAN codes for large-scale scientific computation, http://www.cse.scitech.ac.uk/nag/hsl/.

[21] R. Glowinski, T. W. Pan, T. I. Hesla, and D. D. Joseph, Int. J. Multiphase Flow **25**, 755 (1999).

[22] T. B. Jones, *Electromechanics of Particles* (Cambridge University Press, New York, 1995).

[23] X. Wang, X.-B. Wang, and P. R. C. Gascoyne, J. Electrostat. **39**, 277 (1997).

[24] S. J. Kim and T. H. Kwon, Adv. Polym. Technol. **15**, 41 (1996).

[25] D. S. Kim, S. W. Lee, T. H. Kwon, and S. S. Lee, J. Micromech. Microeng. **14**, 798 (2004).

[26] J. C. Sprott, *Chaos and Time-Series Analysis* (Oxford University Press, Oxford, 2003).

[27] O. S. Galaktionov, P. D. Anderson, G. W. M. Peters, and F. N. van de Vosse, Int. J. Numer. Methods Fluids **32**, 201 (2000).

[28] O. S. Galaktionov, P. D. Anderson, G. W. M. Peters, and H. E. H. Meijer, Can. J. Chem. Eng. **80**, 604 (2002).

[29] P. G. M. Kruijt, O. S. Galaktionov, P. D. Anderson, G. W. M. Peters, and H. E. H. Meijer, AIChE J. **47**, 1005 (2001).

[30] T. G. Kang and T. H. Kwon, J. Micromech. Microeng. **14**, 891 (2004).

[31] P. V. Danckwerts, Appl. Sci. Res. A **3**, 279 (1952).

[32] See EPAPS Document No. E-PLEEE8-76-055712 for the movies corresponding to Fig. 9, showing the progress of mixing via the tracer-tracking method. For more information on EPAPS, see http://www.aip.org/pubservs/epaps.html.